Biomechanics and Modeling in Mechanobiology (2018) 17:1785–1796
https://doi.org/10.1007/s10237-018-1056-1

ORIGINAL PAPER

A numerical study on hemodynamics in the left coronary bifurcation with normal and hypertension conditions

Saeed Bahrami[1] · **Mahmood Norouzi**[1]

Received: 13 January 2018 / Accepted: 12 July 2018 / Published online: 19 July 2018

Abstract
In this study, a three-dimensional analysis of the non-Newtonian blood flow was carried out in the left coronary bifurcation. The Casson model and hyperelastic and rigid models were used as the constitutive equation for blood flow and vessel wall model, respectively. Physiological conditions were considered first normal and then compliant with hypertension disease with the aim of evaluating hemodynamic parameters and a better understanding of the onset and progression of atherosclerosis plaques in the coronary artery bifurcation. Two-way fluid–structure interaction method applying a fully implicit second-order backward Euler differencing scheme has been used which is performed in the commercial code ANSYS and ANSYS CFX (version 15.0). When artery deformations and blood pressure are associated, arbitrary Lagrangian–Eulerian formulation is employed to calculate the artery domain response using the temporal blood response. As a result of bifurcation, noticeable velocity reduction and backflow formation decrease shear stress and made it oscillatory at the starting point of the LCx branch which caused the shear stress to be less than 1 and 2 Pa in the LCx and the LAD branches, respectively. Oscillatory shear index (OSI) as a hemodynamic parameter represents the increase in residence time and oscillatory wall shear stress. Because of using the ideal 3D geometry and realistic physiological conditions, the values obtained for shear stress are more accurate than the previous studies. Comparing the results of this study with previous clinical investigations shows that the regions with low wall shear stress less than 1.20 Pa and with high OSI value more than 0.3 are in more potential risk to the atherosclerosis plaque development, especially in the posterior after the bifurcation.

Keywords Left coronary bifurcation · Casson model · Hypertension disease · Fluid–structure interaction

1 Introduction

Increasing cardiovascular disease has led many researchers to consider investigating the flow of blood through the arteries over the past few decades. An important hemodynamic parameter in determining the location and progress of the cardiovascular disease is wall shear stress (Chaichana et al. 2011; Malvè et al. 2015). This parameter could be obtained by analyzing the variations of the flow in the vicinity of the wall. There are some methods to estimate coronary artery blood flow in vivo which captures speed profiles in the right and left coronary arteries using imaging methods (Johnson et al. 2008; Malvè et al. 2015). It is possible to measure the local position of the plaques, where the minimum wall shear stress occurs, by employing noninvasive methods and simulating computational fluid dynamics (CFD) (Stone et al. 2003). Studies indicated that critical shear stress is associated with the development of arteriosclerosis and hypertension in the areas of coronary artery bifurcation (Chaichana et al. 2013; Eshtehardi et al. 2012; Abbas Nejad et al. 2018; Hiroki et al. 2002; Sun and Cao 2011).

Yin et al. (2011) figured out that when coronary artery endothelial cells are exposed to high shear stress, they tend to be stretched and get aligned with the direction of flow. However, endothelial cells are circularly arranged at lower and oscillating wall shear stress and this will increase a permeability of the blood transmitted particles to the endothelial layers (Chatzizisis et al. 2008; Goubergrits et al. 2008). Farmakis et al. (2004) showed that in places of the coronary artery that has the lower amount of shear stress in endothe-

Electronic supplementary material The online version of this article (https://doi.org/10.1007/s10237-018-1056-1) contains supplementary material, which is available to authorized users.

✉ Mahmood Norouzi
mnorouzi@shahroodut.ac.ir

[1] Faculty of Mechanical Engineering, Shahrood University of Technology, Shahrood, Iran

lial cells, causes growth and development of atherosclerotic plaques. Chatzizisis et al. (2008) pointed out the importance of shear stress changes on the wall and its oscillation in endothelial cells in coronary arteries.

Coronary bifurcation can lead to significant flow disturbances due to convective inertia. These disturbed flows affect various hemodynamic parameters, such as oscillatory shear index (Himburg et al. 2004; Huo et al. 2007). Areas exposed to low shear stress have high OSI values and are more at risk for the accumulation of atherosclerotic plaques (Dabagh et al. 2013; Dong et al. 2013). However, the level of activity of endothelial cells increases in the areas with high shear stress and persuades wall remodeling to abandon degradation of the internal elastic lamina (Liu et al. 2016; Yin et al. 2011). Previous studies have examined the rigid wall and have not considered the tensile properties of the wall in the left coronary bifurcation (Chaichana et al. 2013; Malvè et al. 2015). However, the resilient wall influences on the endothelial cells (Cebral et al. 2002; Lee and Xu 2002).

The fluid–structure interaction (FSI) simultaneously simulates the blood flow effects and arterial wall deformation. Torii et al. (2009) observed a significant difference in instantaneous WSS in rigid and FSI models by examining stenosis flow in the right coronary artery. Huo et al. (2009) obtained the effects of vessel compliance in an animal model of coronary arteries using in vivo measurement and FSI analysis. The studies in the bifurcation of the arteries show that the time-averaged WSS gradient value in the FSI model was always smaller than the rigid model (Dong et al. 2015; Tada and Tarbell 2005).

Studies declared that hypertension, enlargement of smooth muscle cells and increased pulse pressure lead to hardening and rigidity of the wall, as well as the proliferation and production of additional cells. Consequently, structural and mechanical disturbances which cause reduced stiffness and contraction of the arteries are the main attributes of hypertension disease (Arribas et al. 2006; Coogan et al. 2013; Laurent et al. 2005; Matsumoto and Hayashi 1994). Iasiello et al. (2016) observed increased and accumulated low-density lipoprotein (LDL) in vessels with hypertension. Also, wall displacement is significantly influenced by hypertension regardless of disease type and the authors believed that hypertension is a risk factor based on the exhibited FSI results (Lee et al. 2013). Tripathi and Bég (2014) examined the transportation of rheological viscoplastic fluids through physiological vessels by peristalsis. They compared pressure distribution, velocity profiles, friction force and mechanical performance for different viscoplastic liquids. Therefore, the Casson model was considered to provide a relatively precise description of the shear stress–strain specifications of actual biological liquids (Akbar et al. 2016).

In this study, a three-dimensional analysis of the blood flow was carried out using numerical methods of fluid–structure interaction in the bifurcation of the left coronary artery. The wall models were considered rigid and flexible. Boundary conditions were considered normal and associated with hypertension disease. Hence, a better understanding of the onset and progression of atherosclerotic plaques occurs by comparing normal and abnormal models in the coronary artery bifurcation. Since the wall shear stress in the time unit solely does not exhibit high risk areas, the oscillatory shear index changes in arterial regions were investigated by modeling the left coronary artery bifurcation with a resilient wall and applying normal and abnormal conditions.

2 Method of simulation

2.1 Geometry and mesh model

Laboratory measurements have already been performed from special sections of the chest to determine the position of coronary arteries on the normal human heart (Dodge et al. 1988; Steigner et al. 2009). Researchers have provided accurate information on the anatomical status of coronary arteries. This information was obtained from 83 arteriograms from among 9160 consecutive studies that indicated freedom from atherosclerotic disease and consisted of 23 sections of coronary artery, which are commonly used to describe the clinical features of coronary artery disease (Dodge et al. 1992). Each segment or branch is defined by several points during its direction. Each point in the polar coordinates was determined as the radial distance from the coronary entrance and the angle of the patient in the radiographic system. Finally, the points obtained for each part entered a computer-assisted design (CAD) program and the left coronary artery was constructed. The diameters obtained in each section of the left coronary artery are reported in Table 1.

The angiographic information used was related to the end-diastole, so in computational fluid dynamics calculations, the boundary conditions information is appropriated for the

Table 1 Lumen diameters obtained for different parts of the left coronary arteriogram information

Left coronary artery dominant	Lumen diameters (mm)
LM 1	4.6
LM 2	4.6
LM 3	4.5
LAD 1	3.9
LAD 2	3.8
LAD 3	3.7
LCx 1	4
LCx 2	3.9
LCx 3	3.8
LCx 4	3.6

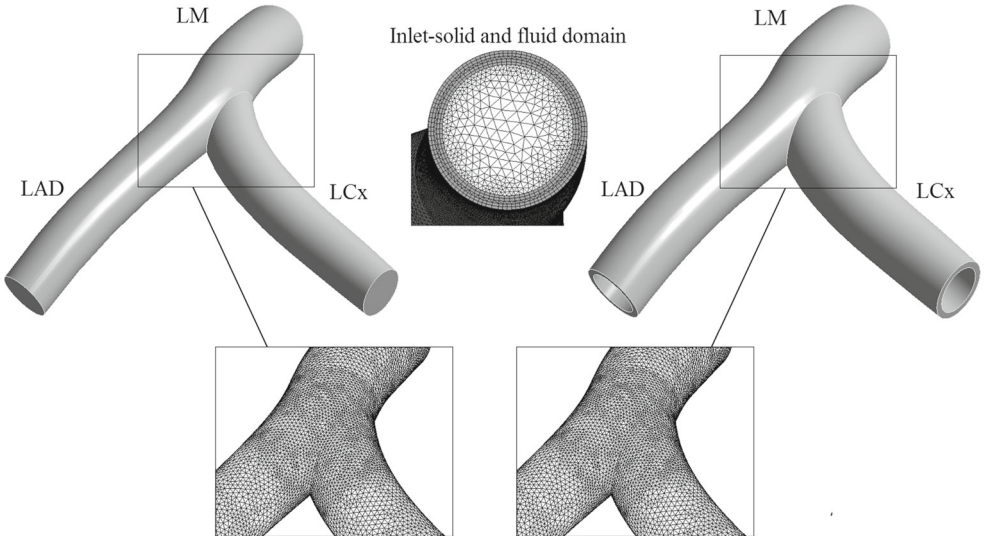

Fig. 1 The three-dimensional geometry with the meshing for the fluid and solid

beginning of the systole phase. This model includes the left main coronary arteries (LM), the left anterior descending (LAD) and the left circumflex artery (LCx).

For coronary artery bifurcation model, both fluid and structural domains have meshed into triangular elements with the reduced combination, which are mostly used to increase the computing performance and numerical convergence associated with large deformation, particularly for soft tissues (Zhao et al. 2012). A division flow location grid refinement was imposed on each model to provide better resolution for branch location quantities. The three-dimensional geometry obtained from arteriogram information along with the mesh for the solid domain of the left coronary artery is shown in Fig. 1.

2.2 Blood flow model

Blood flow in coronary arteries was assumed to be a three-dimensional, time-dependent, isothermal, incompressible, non-Newtonian and laminar flow. The Navier–Stokes equation for this fluid flow is defined as the continuity and the momentum equation as follows (Torii et al. 2007; Norouzi et al. 2018):

$$\frac{\partial u_i}{\partial x_i} = 0 \tag{1a}$$

$$\rho_f \left(\frac{\partial u_i}{\partial t} + u_j \frac{\partial u_i}{\partial x_i} \right) = \frac{\partial \sigma_{ij}}{\partial x_j} + s_i \tag{1b}$$

where t is the time, u_i and σ_{ij} are the components of the velocity vector and stress tensor, respectively, s_i is the component of the momentum source, and ρ_f is blood density that is assumed to be $1060\,\mathrm{kg/m^3}$. The stress tensor components are defined as the following equation (Lee and Xu 2002; Yahya 2010):

$$\sigma_{ij} = -P\delta_{ij} + 2\eta_f d_{ij} \tag{2a}$$

$$d_{ij} = \frac{1}{2}\left(\frac{\partial u_i}{\partial x_j} + \frac{\partial u_j}{\partial x_i} \right) \tag{2b}$$

where P and η_f are the pressure and viscosity of the fluid, respectively, δ_{ij} is the Kronecker delta, and d_{ij} is the deformation rate tensor. Blood flow exhibits the non-Newtonian behavior for the shear rate less than $100\,\mathrm{s^{-1}}$. Casson model is comparatively simple but provide a relatively precise description of the shear stress–strain specifications of actual biological liquids (Akbar et al. 2016). Therefore, for the blood rheology, the Casson model is employed, which can be expressed as follows (Fung 2013; Johnston et al. 2006):

$$\eta_f(\dot{\gamma}) = \left[\left(\frac{\eta_\infty \dot{\gamma}}{2} \right)^{1/2} + 2^{-1/2}\tau_y^{1/2} \right]^2 \frac{2}{\dot{\gamma}}$$
$$\eta_\infty = \eta_0(1 - HCT)^{-\alpha}, \quad \eta_0 = 0.0012\,\mathrm{Pa\,s}$$
$$\tau_y = 0.1(0.625HCT)^3$$
$$\mathrm{HCT} = 0.37 \tag{3}$$

where η_∞ and η_0 are blood viscosity in infinite and zero shear rates, respectively. Also, $\dot{\gamma}$ is the generalized shear rate, HCT is a fractional amount of red blood cells that called hematocrit, and τ_y is yield stress. For human blood, α is 2 and this parameter is obtained using rheological data at the temperature of 37 °C (Das et al. 2000).

2.3 Vessel wall model

The governing equations for the motion of an elastic wall are mathematically defined by the following equation (Torii et al. 2007; Vamerzani et al. 2014):

$$\rho_w \frac{\partial^2 \varepsilon_{ij}}{\partial t^2} = \frac{\partial \sigma_{ij}}{\partial x_j} + \rho_w F_i \tag{4}$$

where ε_{ij} and σ_{ij} are the displacement and stress tensor components in the wall, respectively. ρ_w is the wall density that is assumed to be 1120 kg/m^3, F_i is the body force components that act on the wall, and σ_{ij} can be evaluated from the constitutive equation of the solid material (Chiastra et al. 2016). Wall material deformation is produced as a result of flow, and according to the law of conservation of energy, the energy will store inside the material. Strain energy density function W can be used to measure the energy stored in the material as a result of deformation that can be written as (Cheema and Park 2013):

$$S_{ij} = \frac{\partial W}{\partial \varepsilon_{ij}} = 2\frac{\partial W}{\partial c_{ij}} \tag{5}$$

where S_{ij} is the second Piola–Kirchhoff stress tensor, ε_{ij} and c_{ij} are the Green–Lagrange strain tensor and right Cauchy—Green deformation tensor, respectively. The coronary wall was modeled using a hyperelastic material model called nine parameters Mooney–Rivlin. A hyperelastic material is described as a material that has a conjugate stress component by modifying its elastic potential function with a deformation or strain component. The function of a Mooney–Rivlin material can be written as (Koshiba et al. 2007):

$$\begin{aligned} W = {} & C_1(\bar{I}_1 - 3) + C_2(\bar{I}_2 - 3) + C_3(\bar{I}_1 - 3)^2 \\ & + C_4(\bar{I}_1 - 3)(\bar{I}_2 - 3) + C_5(\bar{I}_2 - 3)^2 + C_6(\bar{I}_1 - 3)^3 \\ & + C_7(\bar{I}_1 - 3)^2(\bar{I}_2 - 3) + C_8(\bar{I}_1 - 3)(\bar{I}_2 - 3)^2 \\ & + C_9(\bar{I}_2 - 3)^3 + \frac{1}{d}(J-1)^2 \end{aligned} \tag{6}$$

where $C_{1\text{–}9}$ are so-called Mooney–Rivlin constants, d is material incompressibility parameter, J is the ratio of the deformed elastic volume to the inconvertible volume; $\bar{I}_1 = I_1/I_3^{1/3}$ and $\bar{I}_2 = I_2/I_3^{2/3}$ are first and second deviatoric strain invariant, respectively. If the principal stretches of the material are denoted λ_1, λ_2 and λ_3 can be written as the strain definitions for the substance as follows (Karimi et al. 2014):

$$\bar{I}_1 = \lambda_1^2 + \lambda_2^2 + \lambda_3^2 \tag{7a}$$

$$\bar{I}_2 = \lambda_1^2\lambda_2^2 + \lambda_1^2\lambda_3^2 + \lambda_2^2\lambda_3^2 \tag{7b}$$

$$\bar{I}_3 = \lambda_1^2\lambda_2^2\lambda_3^2 \tag{7c}$$

The inner walls of the arteriole that are in direct contact with the blood take the load and the total stress distribution was computed during fluid dynamic analysis. Arterial tissue in the present study supposed incompressible. In other words, the third deviatory strain is unchangeable ($\bar{I}_3 = 1$). The Mooney–Rivlin constants for the healthy human coronary arteries which were obtained from the experimental test on coronary arteries are $C_1 = 0.070$, $C_3 = 3.2$, $C_7 = 0.07160$ and C_i=0.0 (i=2, 4, 5, 6, 8 and 9) MPa and $d = 10^{-5}$ Pa^{-1} (Koshiba et al. 2007).

2.4 Boundary conditions

In this study, the three-dimensional geometry of the left coronary artery was regarded. Blood was also considered as a non-Newtonian fluid and interacts with the hyperelastic homogeneous artery. The pulsatile coronary pressure was applied as an inlet boundary condition at the entrance of LM, and pulsatile velocity was assumed on both the LAD and the LCx outlet boundaries. The volumetric flow was obtained using the Murray low of discharge at each outlet because it is associated with the inlet of the clinical data of the coronary arteries. This law articulates that the optional radius of a blood vessel is proportional to vessel flow to the third power (Murasato et al. 2010; Murray 1926). Blood flow in the coronary artery is guided by a combination of aortic pressure and downstream coronary artery resistance. However, during the systole, distal coronary artery resistance increases significantly as a result of increased myocardial pressure due to cardiac contraction. The myocardial pressure depends on the aorta flow and ventricular pressure. Hence, there is an interaction between the boundary conditions in the aortic and coronary flow (Coogan et al. 2013; Sengupta et al. 2012). The inlet and outlet boundary conditions are shown in Fig. 2, and they are based on a physiological pulsatile flow rate and pressure at the coronary for normal and hypertension models (Nichols et al. 2011; Wiwatanapataphee et al. 2012).

The heartbeat causes effects on the flow of the vessels, so there are accurate data on the movement of the heart (Xavier et al. 2012). Coronary artery on the heart is affected by this movement. Studies have been made using a modified phase-based optical flow method that estimates the motion of a local myocardial. The estimated speed was calculated in 11 healthy subjects in peak systole and diastole. The peak systole and diastole velocity appear at 27 and 66% of the cardiac cycle, respectively. Considering the position of the left coronary artery, the effects of the movement of the heart wall on the vessels were considered along with the anterior, lateral and septum axis. Figure 3 presents the evolution of the radial velocity of the septal, lateral and anterior segments on the short-axis orientations along the entire cardiac cycle.

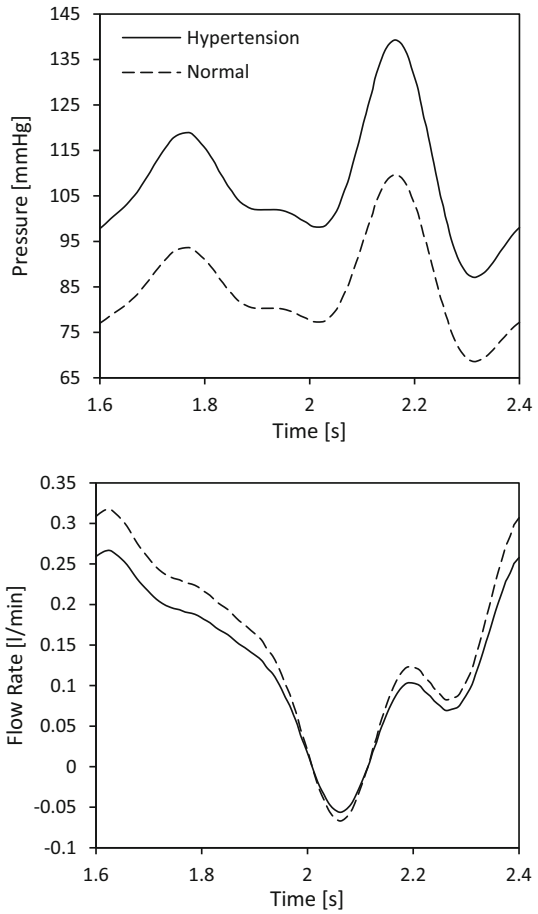

Fig. 2 Pulsatile blood flow waves used in this study for normal and hypertension models

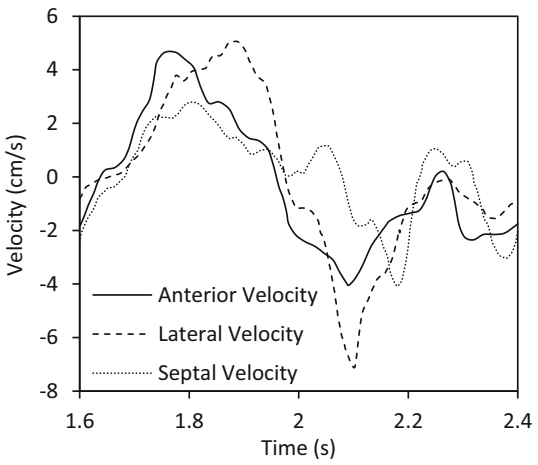

Fig. 3 Velocity curves along the cardiac cycle expressed at the septal, lateral and anterior segments of normal heart examination

2.5 Definition of oscillatory shear index

Ku et al. (1985) found an influential relationship between plaque location and oscillating shear stress, showing that marked oscillations in the direction of wall shear may advance atherogenesis. Consequently, they put forward the concept of the oscillatory shear index to quantify the oscillatory nature of WSS. The modified definition of OSI is given as (He and Ku 1996; Ku et al. 1985):

$$\mathrm{OSI} = 0.5 \times \left(1 - \frac{\left|\int_0^T \bar{\tau} \cdot \mathrm{d}t\right|}{\int_0^T |\bar{\tau}| \cdot \mathrm{d}t}\right) \tag{8}$$

where T is the time period of a cardiac cycle and $\bar{\tau}$ is the WSS vector. This definition takes into account not only the reverse (180°) direction but also any direction changes (0°–180°) of the WSS in three-dimensional space. The OSI value varies between 0 and 0.5, where 0 corresponds to the regions experiencing no backward flow, and 0.5 is for the case of fully oscillatory flow without net forward flow.

2.6 Numerical method

A two-way fluid–structure interaction simulation of blood flow in coronary artery bifurcation models is conducted using a fully implicit second-order backward Euler differencing scheme by the commercial computational software ANSYS Workbench (ANSYS Inc.). The fully coupled FSI models were solved in ANSYS CFX and ANSYS Mechanical. ANSYS CFX is finite-volume-based software for fluid mechanics computations and uses a non-staggered grid layout such that the control volumes are exactly alike for all carrier equations. ANSYS Mechanical is finite-element-based software for structural mechanical analysis. FSI models are coupled and determined iteratively by these two packages within each time step by applying appropriate boundary conditions at the fluid–structure interface until the coupling system residual is less than a specified tolerance. Since blood domain has moving boundaries, an arbitrary Lagrangian–Eulerian (ALE) formulation is used for the analysis of the fluid flow. This formulation can be directly coupled with the Lagrangian formulation of the artery domain. For each coronary artery model, transient flow simulations at three cardiac cycles were performed, and results in the last cycle were used for mechanical and hemodynamic analysis. A regular time step equal to 0.005 s with 160 total times step cardiac cycle was employed. The convergence criterion is set to 10^{-5} in this study.

The grid independency is defined on the basis of a mesh density study on the normal model using four mesh sizes, and the peak diastole WSS values at the beginning of the LAD branch are compared. The number of elements in these grids for the structural domain is M1 = 31227, M2 = 79451, M3 = 188514 and M4 = 353788. Figure 4 shows the grid independency study at WSS values are refinements at the peak of diastole phase.

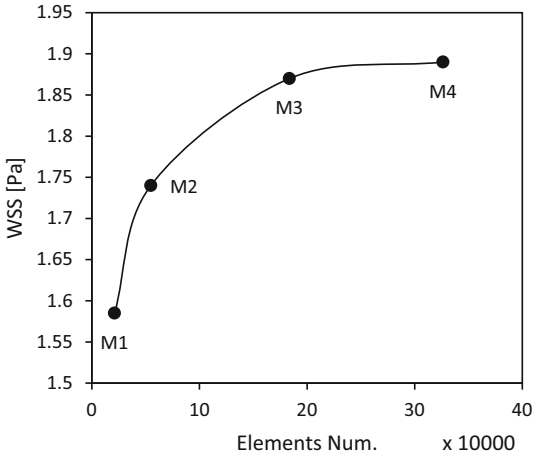

Fig. 4 Grid independency study at WSS value

For a more thorough investigation of the numerical resolution of grid independency, the results are reported as a standard error among the created grids. Percentage of the available error between the M3 and M4 meshes at the beginning of the LAD is about 0.85%. However, in the other two grids, the error rate increases to 16.35 percent. Here, M3 is considered as the reference grid because it has a lower CPU time and error rate than the M4 (less than 1%).

3 Results and discussion

The hemodynamic parameters were evaluated for different models at specified times and locations. The velocity reduces by bifurcating of flow at the beginning of the LAD and LCx branches. Since the deviation angle of the branch of the LCx is higher than the LAD, the velocity in this branch decreases further. The mean velocity decreased by 42.34% at the beginning of the LCx branch compared to the LAD branch in the normal hyperelastic model and at the peak systole. These values for hypertension and rigid models are 40.44 and 34.41, respectively. Figure 5 shows the velocity profiles at the beginning of the LCx and LAD branches at the peak systole for different models.

The difference of average velocity between hyperelastic-hypertension and hyperelastic-normal models is 15.96% at the beginning of the LCx branch, while the difference of average velocity increased to 17.18% in the hyperelastic-normal and rigid-normal models. Also, at the beginning of the LAD branch, the difference of average velocity between hyperelastic-hypertension and hyperelastic-normal models is 18.65%, while the error between the hyperelastic-normal and rigid-normal models is 3.4%. Figure 6 shows velocity contours at three cross sections of coronary bifurcation and in different models at the peak systole and diastole. The peak systole occurs at maximum velocity and after the bifurcating a slowdown happens at the beginning of the LCx and LAD branches. At this time, the slowdown was observed in the posterior region in the branches of LAD and LCx. In the hypertension model, the lowest velocity was discerned compared to other models. At the peak diastole, backflow is attended, especially on the wall. At this time, the velocity in the posterior region was the highest in the branches of LAD and LCx and there were backflow and vortex flow in these regions.

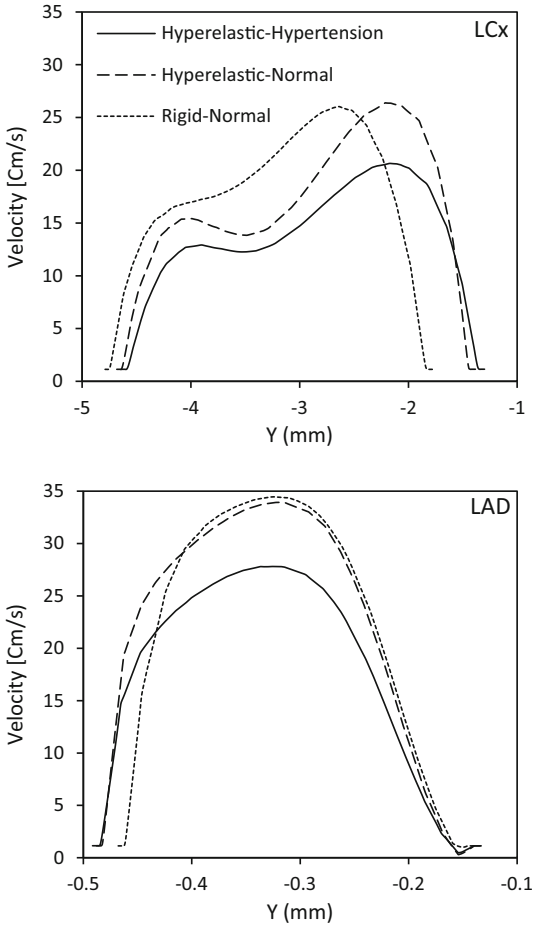

Fig. 5 Velocity profiles in peak systole for different models

In order to better understand the backflow and vortex flow, the velocity vectors are obtained in the bifurcation site and at the peak diastole. As seen in Fig. 7, there are considerable backflow and vortex flow at the beginning of the LAD and LCx branches. In the LCx branch, especially in the hypertension model, the larger vortex flow is compared to other models.

WSS is the most important parameter in the study of atherosclerosis. Hence, the LM branch and its tributaries are used to investigate variations of this parameter. Figure 8 shows the WSS for a cardiac cycle in different models at the end of the LM branch. According to Fig. 8,

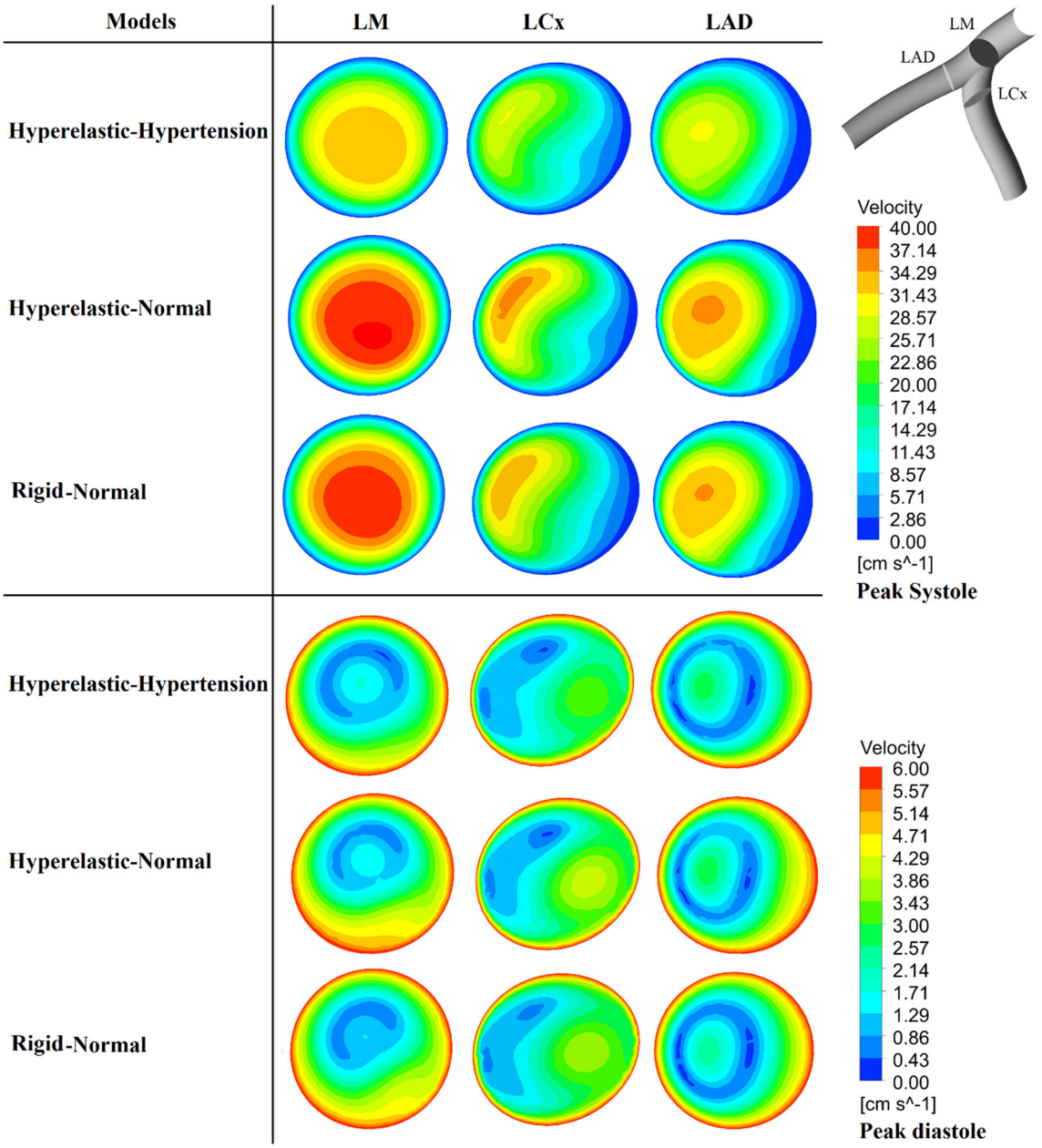

Fig. 6 Velocity contours in three coronary positions for different models at the peak systole and diastole

there is 22.92% difference at WSS magnitude between hyperelastic-hypertension and hyperelastic-normal models, while this amount reduced to 4.58% in the hyperelastic-normal and rigid-normal models. The maximum WSS in Fig. 8 is 2.56 Pa at the beginning of the systole phase in the hyperelastic-normal model. In rigid and hypertension models, the maximum WSS is reduced to 2.43 and 1.97 Pa, respectively.

Due to the flow division and decreasing the velocity, we expected to reduce the WSS at the beginning of the branches of LCx and LAD. Figure 9 shows the wall shear stress magnitude at the beginning of LCx for different models. In this area, the WSS is different for hyperelastic models about 12% and for normal models 5%. According to the figure, there is low shear stress at the beginning of the LCx branch. Also, the results show high oscillations and low shear stress at the beginning of the LAD branch. In this area, the difference of WSS magnitude between hyperelastic-hypertension and hyperelastic-normal models is 29.62%, while the difference of WSS magnitude increased to 31.7% in the hyperelastic-normal and rigid-normal models.

Figure 10 shows the wall shear stress magnitude at the beginning of LAD for different models. The maximum WSS

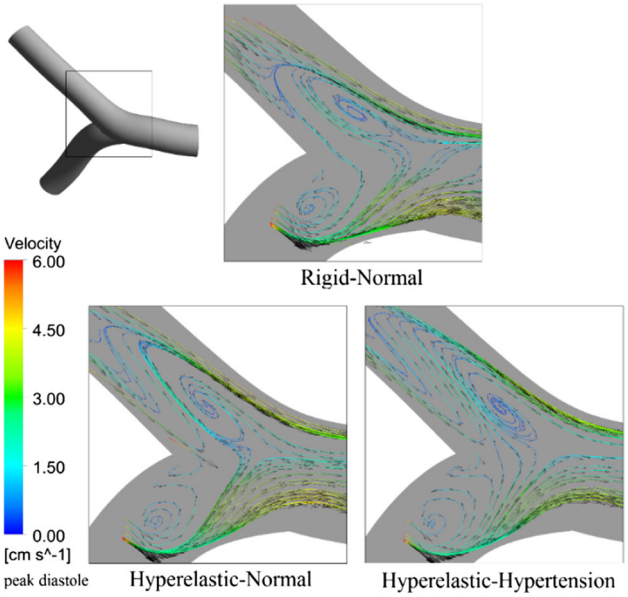

Fig. 7 Velocity vectors at the coronary bifurcation and in different models at the peak diastole

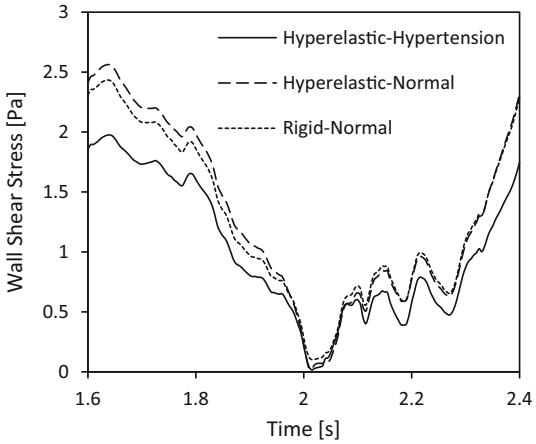

Fig. 8 WSS for different models at the end of the LM branch

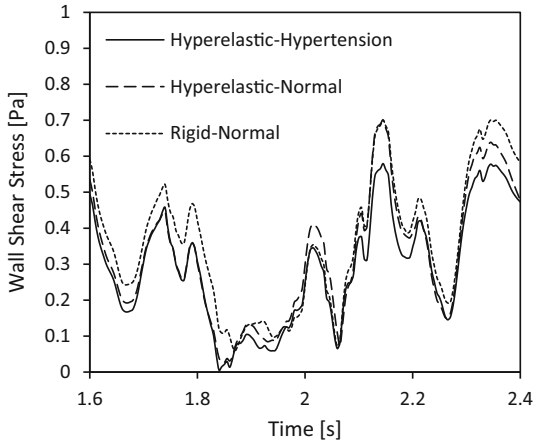

Fig. 9 WSS for different models at the beginning of the LCx branch

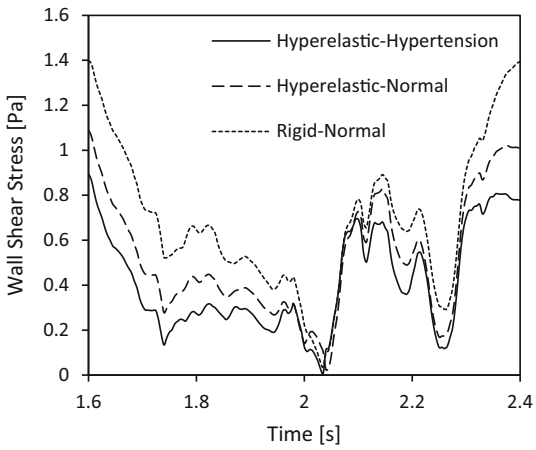

Fig. 10 WSS for different models at the beginning of the LAD branch

at the end of the diastole phase and in the rigid model in Figs. 9 and 10 is 0.7 and 1.43 Pa, respectively.

The results of shear stress magnitude indicate that in addition to lower WSS at the beginning of the branches of LAD and LCx, oscillatory WSS also occurs. Whereas these values are opposite to each other in the anterior and posterior positions. Figure 11 shows the wall shear stress magnitude in the normal hyperelastic model in the anterior and posterior positions of the left coronary arteries. As seen in the normal hyperelastic model, the low and oscillatory shear stress occurred more in the posterior positions of the coronary artery. Shear stress magnitude reduced due to the presence of curvature after coronary bifurcation and backflow into the vessels. The shear stress difference in the anterior and posterior positions is 61.88 and 68.07% at the beginning of LAD and LCx, respectively. Since LM branch is undeviating, the shear stress magnitude in the anterior and posterior positions of this branch is approximately the same and there are very low backflow and vortex in this section.

Figure 12 shows the shear stress contour for the different models at peak systole and diastole. The results show the maximum and minimum shear stress on the wall. Whereas when peak diastole occurs the shear stress is lowest and this amount of shear stress is undesirable and is the main cause of atherosclerosis disease. Therefore, by considering the oscillatory shear index, WSS can be expressed independently of time.

Shear stress changes at different times and this information are not sufficient to diagnose the disease; so the oscillatory shear index (OSI) parameter is expressed. The high OSI values express the low shear stress and oscillatory that this parameter can be used as a diagnosis of the disease. Figure 13 demonstrates the oscillatory shear index values in different wall models. As seen, high OSI values are at the beginning of the coronary bifurcation, and immediately reduce these val-

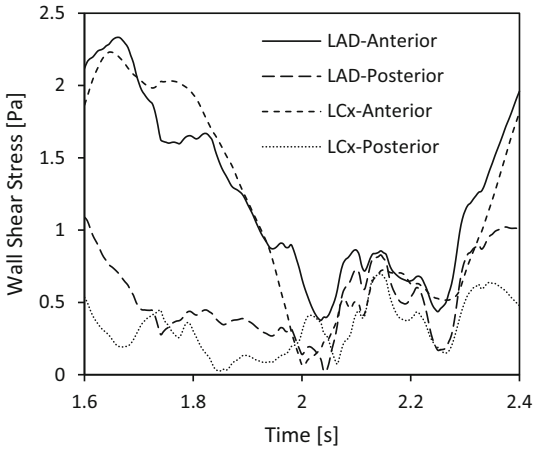

Fig. 11 WSS magnitude in the normal hyperelastic model at the anterior and posterior position of left coronary arteries

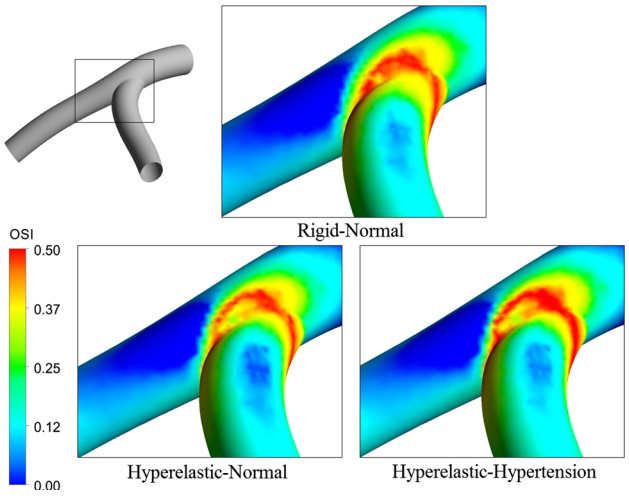

Fig. 13 Oscillatory shear index contour for different models

ues after bifurcation. For the hypertension model, the OSI is about 0.4–0.5 at the coronary bifurcation, while these values are about 0.35–0.45 for normal models. High OSI occurred in the bifurcation site because of the presence of backflow and the rapid reduction in the velocity values, which then with developing average velocity, the shear stress increased and decreased the OSI.

The largest displacement in the wall occurred in the hypertension model in the LCx branch due to high pressure in the artery. The difference of wall motion between hyperelastic-hypertension and hyperelastic-normal models and at peak systole and at the LCx and LAD branches are 26.65 and 19.76%, respectively. Figure 14 shows the displacement of the wall in hyperelastic models in the peak systole for the LCx and LAD branches. Regarding the wall motion in resilient models, it is observed that with increasing physiological pressure, the wall motion increases. In the LCx branch, there was a higher displacement than the LAD branch, due to the higher frequency of movement in this area of the coronary arteries.

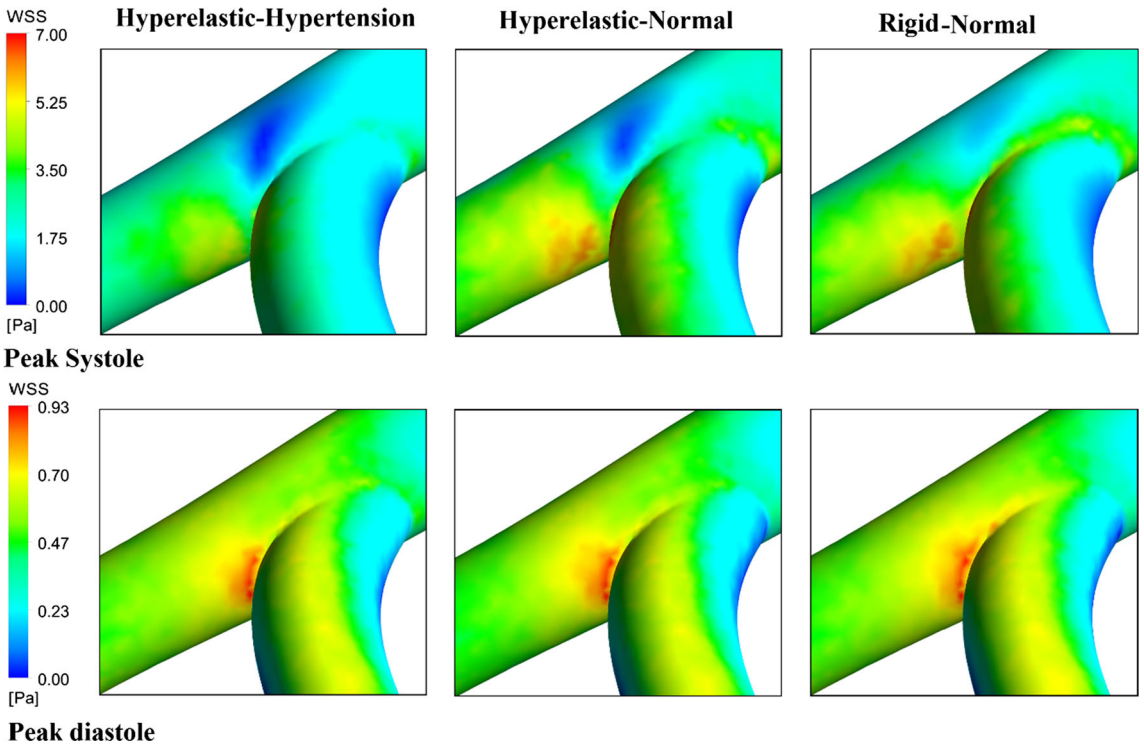

Fig. 12 Shear stress contour for the different models at peak systole and diastole

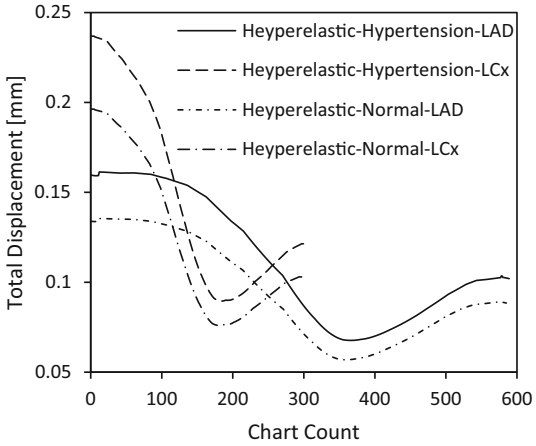

Fig. 14 Total displacement in the LCx and LAD branches at the peak systole

4 Conclusions

In this study, the pulsatile flow of non-Newtonian fluid in the left coronary bifurcation and applied the healthy and unhealthy physiology conditions with the effect of fluid–structure interaction is studied. In past studies, using the computational and clinical analysis, the distribution of wall shear stress and its oscillation in coronary arteries were investigated (Nordgaard et al. 2010; Soulis et al. 2006). Changing the direction of the wall shear stress vectors due to the high OSI increases the production of the gene endothelin-1 mRNA, and it causes cell proliferation on the vascular (Chiastra et al. 2013). In other words, shear stress is not a comprehensive explanation for the permeability of blood-borne particles, and differences in OSI change permeability level (Himburg et al. 2004). Recent studies have shown 25% difference between shear stress in the resilient arteries and rigid ones (Cebral et al. 2002). Comparing flow in rigid and hyperelastic walls, one can have a better perception of flow changes.

Clinical results achieved in recent years confirm that most of the coronary artery stenosis occurs in this area with low shear stress (Chatzizisis et al. 2008; Karimi et al. 2014; Sadeghi et al. 2011). These studies show the wall vulnerability based is on peak plaque stress using human samples and critical WSS in the range of 0.7–1.2 Pa at the site of coronary which is consistent with the results obtained in this study. According to clinical and numerical studies in recent years, these areas have the highest risk of developing atherosclerotic plaques (Karimi et al. 2014; Nichols et al. 2011; Papafaklis et al. 2010). In this study, we observed the difference between rigid and resilient models.

The difference of average velocity between hyperelastic-normal and rigid-normal models is 3.04 and 17.18% at the beginning of the LAD and LCx branches, respectively. Here, the percentage of error is defined as the ratio of the absolute difference of average velocity of two models to the mean of them. At the beginning of the LAD branch due to the alignment with the LM were observed slight variations between the rigid and normal hyperelastic models. The hardening of the wall increases the wave propagation and reduces the time difference between the pressure at the inlet and the outlet (Jarvinen et al. 2001). According to the Poiseuille equation, the flow rate is related to the fourth power of the radius and decreasing the elasticity of the wall causes to reduce the velocity. The wall shear stress fluctuates due to shear rate variation as a result of velocity change near the wall. It also affects the results accuracy of 25% variation in the different wall models (Cebral et al. 2002; Penrose et al. 2000). Shear stress is severely reduced after bifurcation. This reduction in WSS due to backflow and vortex which causes shear stress oscillation and high OSI values of about 0.35–0.5 which possibility increases of plaque production in these areas.

The lowest amount of wall shear stress is seen in the hypertension model. In the LM branch due to the existence of a fully developed flow, the shear stress magnitude has the highest value and has fewer oscillate. The decrease in velocity and backflow formation due to the coronary bifurcation and significant decrease occurred in shear stress and made it oscillatory at the starting point of the LCx branch which caused the shear stress to be less than 1 Pa. In the LAD branch, the shear stress is reduced due to bifurcation and backflow to be less than 2 Pa. Regarding to the curvature, the shear stress magnitude in the posterior region is significantly different from the anterior at the beginning of the branches of LAD and LCx, so that the lowest shear stress and the highest oscillating shear stress occurred in the posterior region at the left coronary bifurcation. The differences of shear stress in the anterior and posterior positions are 61.88 and 68.07% at the beginning of LAD and LCx, respectively.

Because of considering the 3D geometry and using the physiological boundary conditions, the correct values were obtained for WSS in the left coronary bifurcation. The results have been consistent with the clinical and numerical studies of previous investigations. It can be concluded that the highest potential risk for atherosclerosis disease is in the regions with low wall shear stress less than 1.20 Pa and with high OSI value more than 0.3. In other words, it is better to use high OSI values to express the risk of diseases.

For future studies, using real geometry obtained from CT-scan images instead of the ideal geometry is recommended. Different models, such as viscoelastic walls, could be utilized to improve wall deformability, and the effect of stenosis for different parts of the coronary artery bifurcation with various non-Newtonian blood models could be studied. It is also recommended to examine the effects of multilayer walls and LDL in blood flow.

References

Abbas Nejad A, Talebi Cheraghali D, Shahbani-Zahiri A, Norouzi M (2018) Pulsatile flow of non-Newtonian blood fluid inside stenosed arteries: investigating the effects of viscoelastic and elastic walls, arteriosclerosis, and polycythemia diseases. Comput Methods Programs Biomed 154:109–122

Akbar NS, Tripathi D, Bég OA, Khan Z (2016) MHD dissipative flow and heat transfer of Casson fluids due to metachronal wave propulsion of beating cilia with thermal and velocity slip effects under an oblique magnetic field. Acta Astronaut 128:1–12

Arribas SM, Hinek A, González MC (2006) Elastic fibres and vascular structure in hypertension. Pharmacol Ther 111:771–791

Cebral JR, Yim PJ, Löhner R, Soto O, Choyke PL (2002) Blood flow modeling in carotid arteries with computational fluid dynamics and MR imaging. Acad Radiol 9:1286–1299

Chaichana T, Sun Z, Jewkes J (2011) Computation of hemodynamics in the left coronary artery with variable angulations. J Biomech 44:1869–1878

Chaichana T, Sun Z, Jewkes J (2013) Hemodynamic impacts of various types of stenosis in the left coronary artery bifurcation: a patient-specific analysis. Physica Med 29:447–452

Chatzizisis YS et al (2008) Prediction of the localization of high-risk coronary atherosclerotic plaques on the basis of low endothelial shear stress. Circulation 117:993–1002

Cheema TA, Park CW (2013) Numerical investigation of hyperelastic wall deformation characteristics in a micro-scale stenotic blood vessel Korea-Australia. Rheol J 25:121–127

Chiastra C, Morlacchi S, Gallo D, Morbiducci U, Cárdenes R, Larrabide I, Migliavacca F (2013) Computational fluid dynamic simulations of image-based stented coronary bifurcation models. J R Soc Interface 10:20130193

Chiastra C et al (2016) Computational replication of the patient-specific stenting procedure for coronary artery bifurcations: from OCT and CT imaging to structural and hemodynamics analyses. J Biomech 49:2102–2111

Coogan JS, Humphrey JD, Figueroa CA (2013) Computational simulations of hemodynamic changes within thoracic, coronary, and cerebral arteries following early wall remodeling in response to distal aortic coarctation. Biomech Model Mechanobiol 12:79–93

Dabagh M, Takabe W, Jalali P, White S, Jo H (2013) Hemodynamic features in stenosed coronary arteries: CFD analysis based on histological images. J Appl Math 2013:1–11

Das B, Johnson P, Popel A (2000) Computational fluid dynamic studies of leukocyte adhesion effects on non-Newtonian blood flow through microvessels. Biorheology 37:239–258

Dodge JT, Brown BG, Bolson EL, Dodge HT (1988) Intrathoracic spatial location of specified coronary segments on the normal human heart. Applications in quantitative arteriography, assessment of regional risk and contraction, and anatomic display. Circulation 78:1167–1180

Dodge JT, Brown BG, Bolson EL, Dodge HT (1992) Lumen diameter of normal human coronary arteries. Influence of age, sex, anatomic variation, and left ventricular hypertrophy or dilation. Circulation 86:232–246

Dong J, Wong KK, Tu J (2013) Hemodynamics analysis of patient-specific carotid bifurcation: a CFD model of downstream peripheral vascular impedance. Int J Numer Method Biomed Eng 29:476–491

Dong J, Sun Z, Inthavong K, Tu J (2015) Fluid–structure interaction analysis of the left coronary artery with variable angulation. Comput Methods Biomech Biomed Engin 18:1500–1508

Eshtehardi P et al (2012) Association of coronary wall shear stress with atherosclerotic plaque burden, composition, and distribution in patients with coronary artery disease. J Am Heart Assoc 1:e002543

Farmakis TM, Soulis JV, Giannoglou GD, Zioupos GJ, Louridas GE (2004) Wall shear stress gradient topography in the normal left coronary arterial tree: possible implications for atherogenesis. Curr Med Res Opin 20:587–596

Fung Y-C (2013) Biomechanics: mechanical properties of living tissues. Springer, Berlin

Goubergrits L, Kertzscher U, Schöneberg B, Wellnhofer E, Petz C, Hege H-C (2008) CFD analysis in an anatomically realistic coronary artery model based on non-invasive 3D imaging: comparison of magnetic resonance imaging with computed tomography. Int J Cardiovasc Imaging 24:411–421

He X, Ku DN (1996) Pulsatile flow in the human left coronary artery bifurcation: average conditions. J Biomech Eng 118:74–82

Himburg HA, Grzybowski DM, Hazel AL, LaMack JA, Li X-M, Friedman MH (2004) Spatial comparison between wall shear stress measures and porcine arterial endothelial permeability. Am J Physiol Heart Circ Physiol 286:H1916–H1922

Hiroki M, Miyashita K, Oda M (2002) Tortuosity of the white matter medullary arterioles is related to the severity of hypertension. Cerebrovasc Dis 13:242–250

Huo Y, Wischgoll T, Kassab GS (2007) Flow patterns in three-dimensional porcine epicardial coronary arterial tree. Am J Physiol Heart Circ Physiol 293:H2959–H2970

Huo Y, Choy JS, Svendsen M, Sinha AK, Kassab GS (2009) Effects of vessel compliance on flow pattern in porcine epicardial right coronary arterial tree. J Biomech 42:594–602

Iasiello M, Vafai K, Andreozzi A, Bianco N (2016) Low-density lipoprotein transport through an arterial wall under hyperthermia and hypertension conditions—an analytical solution. J Biomech 49:193–204

Jarvinen E, Lyly M, Ruokolainen J, Raback P (2001) Three-dimensional fluid-structure interaction modeling of blood flow in elastic arteries. In: ECCOMAS Comp fluid dynamics conference, Swansea, Wales, UK

Johnson K, Sharma P, Oshinski J (2008) Coronary artery flow measurement using navigator echo gated phase contrast magnetic resonance velocity mapping at 3.0 T. J Biomech 41:595–602

Johnston BM, Johnston PR, Corney S, Kilpatrick D (2006) Non-Newtonian blood flow in human right coronary arteries: transient simulations. J Biomech 39:1116–1128

Karimi A, Navidbakhsh M, Shojaei A, Hassani K, Faghihi S (2014) Study of plaque vulnerability in coronary artery using Mooney-Rivlin model: a combination of finite element and experimental method. Biomed Eng Appl Basis Commun 26:1450013

Koshiba N, Ando J, Chen X, Hisada T (2007) Multiphysics simulation of blood flow and LDL transport in a porohyperelastic arterial wall model. J Biomech Eng 129:374–385

Ku DN, Giddens DP, Zarins CK, Glagov S (1985) Pulsatile flow and atherosclerosis in the human carotid bifurcation. Positive correlation between plaque location and low oscillating shear stress. Arterioscler Thromb Vasc Biol 5:293–302

Laurent S, Boutouyrie P, Lacolley P (2005) Structural and genetic bases of arterial stiffness. Hypertension 45:1050–1055

Lee K, Xu X (2002) Modelling of flow and wall behaviour in a mildly stenosed tube. Med Eng Phys 24:575–586

Lee C-J, Zhang Y, Takao H, Murayama Y, Qian Y (2013) A fluid–structure interaction study using patient-specific ruptured and unruptured aneurysm: the effect of aneurysm morphology, hypertension and elasticity. J Biomech 46:2402–2410

Liu J, Jing L, Wang C, Zhang Y, Yang X (2016) Recanalization, regrowth, and delayed rupture of a previously coiled unruptured anterior communicating artery aneurysm: a longitudinal hemodynamic analysis. World Neurosurg 89:726

Malvè M, Gharib A, Yazdani S, Finet G, Martínez M, Pettigrew R, Ohayon J (2015) Tortuosity of coronary bifurcation as a potential local risk factor for atherosclerosis: CFD steady state study based on in vivo dynamic CT measurements. Ann Biomed Eng 43:82–93

Matsumoto T, Hayashi K (1994) Mechanical and dimensional adaptation of rat aorta to hypertension. J Biomech Eng 116:278

Murasato Y et al (2010) Recent perspective on coronary bifurcation intervention: statement of the "Bifurcation Club in KOKURA". J Interv Cardiol 23:295–304

Murray CD (1926) The physiological principle of minimum work I. The vascular system and the cost of blood volume. Proc Natl Acad Sci 12:207–214

Nichols W, O'Rourke M, Vlachopoulos C (2011) McDonald's blood flow in arteries: theoretical, experimental and clinical principles. CRC Press, Cambridge

Nordgaard H et al (2010) Impact of competitive flow on wall shear stress in coronary surgery: computational fluid dynamics of a LIMA–LAD model. Cardiovasc Res 88:512–519

Norouzi M, Jafari A, Mahmoudi M (2018) A numerical study on nonlinear dynamics of three-dimensional time-depended viscoelastic Taylor-Couette flow. Rheol Acta 57:127–140

Papafaklis MI, Koskinas KC, Chatzizisis YS, Stone PH, Feldman CL (2010) In-vivo assessment of the natural history of coronary atherosclerosis: vascular remodeling and endothelial shear stress determine the complexity of atherosclerotic disease progression. Curr Opin Cardiol 25:627–638

Penrose J, Hose D, Staples C, Hamill I, Jones I, Sweeney D (2000) Fluid structure interactions: coupling of CFD and FE. In: 18th CAD-FEM user's meeting-international congress on FEM technology

Sadeghi M, Shirani E, Tafazzoli-Shadpour M, Samaee M (2011) The effects of stenosis severity on the hemodynamic parameters—assessment of the correlation between stress phase angle and wall shear stress. J Biomech 44:2614–2626

Sengupta D, Kahn AM, Burns JC, Sankaran S, Shadden SC, Marsden AL (2012) Image-based modeling of hemodynamics in coronary artery aneurysms caused by Kawasaki disease. Biomech Model Mechanobiol 11:915–932

Soulis JV, Farmakis TM, Giannoglou GD, Louridas GE (2006) Wall shear stress in normal left coronary artery tree. J Biomech 39:742–749

Steigner ML et al (2009) Iodinated contrast opacification gradients in normal coronary arteries imaged with prospectively ECG-gated single heart beat 320-detector row computed tomography. Circ Cardiovas Imaging CIRCIMAGING 109.854307

Stone PH et al (2003) Effect of endothelial shear stress on the progression of coronary artery disease, vascular remodeling, and in-stent restenosis in humans. Circulation 108:438–444

Sun Z, Cao Y (2011) Multislice CT angiography assessment of left coronary artery: correlation between bifurcation angle and dimensions and development of coronary artery disease. Eur J Radiol 79:e90–e95

Tada S, Tarbell J (2005) A computational study of flow in a compliant carotid bifurcation–stress phase angle correlation with shear stress. Ann Biomed Eng 33:1202–1212

Torii R, Oshima M, Kobayashi T, Takagi K, Tezduyar TE (2007) Influence of wall elasticity in patient-specific hemodynamic simulations. Comput Fluids 36:160–168

Torii R et al (2009) Fluid–structure interaction analysis of a patient-specific right coronary artery with physiological velocity and pressure waveforms Int J Numer Method. Biomed Eng 25:565–580

Tripathi D, Bég OA (2014) Mathematical modelling of peristaltic propulsion of viscoplastic bio-fluids. Proc Inst Mech Eng Part H J Eng Med 228:67–88

Vamerzani BZ, Norouzi M, Firoozabadi B (2014) Analytical solution for creeping motion of a viscoelastic drop falling through a Newtonian fluid Korea-Australia. Rheol J 26:91–104

Wiwatanapataphee B, Wu YH, Siriapisith T, Nuntadilok B (2012) Effect of branchings on blood flow in the system of human coronary arteries. Math Biosci Eng 9:199–214

Xavier M, Lalande A, Walker PM, Brunotte F, Legrand L (2012) An adapted optical flow algorithm for robust quantification of cardiac wall motion from standard cine-mr examinations. IEEE Trans Inf Technol Biomed 16:859–868

Yahya M (2010) Three dimensional finite-element modeling of blood flow in elastic vessels: effects of arterial geometry and elasticity on aneurysm growth and rupture. Ryerson University, p 486

Yin W, Shanmugavelayudam SK, Rubenstein DA (2011) The effect of physiologically relevant dynamic shear stress on platelet and endothelial cell activation. Thromb Res 127:235–241

Zhao S, Gu L, Froemming SR (2012) Finite element analysis of the implantation of a self-expanding stent: impact of lesion calcification. J Med Devices 6:021001